ELSEVIER

Chemical Engineering Science 59 (2004) 525–541

Chemical Engineering Science

www.elsevier.com/locate/ces

Comparison of contact-force models for the simulation of collisions in DEM-based granular flow codes

Alberto Di Renzo*, Francesco Paolo Di Maio

Dipartimento di Ingegneria Chimica e dei Materiali, Università della Calabria, Via P. Bucci, cubo 44a, I 87030 Rende (CS), Italy

Received 13 March 2003; received in revised form 30 June 2003; accepted 14 September 2003

Abstract

The distinct element method (DEM) has proven to be reliable and effective in characterizing the behavior of particles in granular flow simulations. However, in the past, the influence of different force–displacement models on the accuracy of the simulated collision process has not been well investigated. In this work, three contact force models are applied to the elementary case of an elastic collision of a sphere with a flat wall. The results are compared, on a macroscopic scale, with the data provided by the experiments of Kharaz et al. (Powder Technol. 120 (2001) 281) and, on a microscopic scale, with the approximated analytical solution derived by Maw et al. (Wear 38 (1976) 101. The force–displacement models considered are: a linear model, based on a Hooke-type relation; a non-linear model, based on the Hertz theory (J. Reine Angew. Math. 92 (1882) 156) for the normal direction and the no-slip solution of the theory developed by Mindlin and Deresiewicz (Trans. ASME. Ser. E, J. Appl. Mech. 20 (1953) 327) for the tangential direction; a non-linear model with hysteresis, based on the complete theory of Hertz and Mindlin and Deresiewicz for elastic frictional collisions. All the models are presented in fully displacement-driven formulation in order to allow a direct inclusion in DEM-based codes.

The results show that, regarding the values of the velocities at the end of collision, no significant improvements can be attained using complex models. Instead, the linear model gives even better results than the no-slip model and often it is equivalent to the complete Mindlin and Deresiewicz model. Also in the microscopic scale, the time evolution of the tangential forces, velocities and displacements predicted by the linear model shows better agreement with the theoretical solution than the no-slip solution. However, this only happens if the parameters of the linear model are precisely evaluated.

The examination of the evolution of the forces, velocities and displacements during the collision emphasizes the importance of correct accounting for non-linearity in the contact model and micro-slip effects. It also demonstrates how these phenomena need to be considered into the model in order to perform deeper analyses on granular material in motion and, in general, for systems sensitive to the actual force or displacement. For these cases, more accurate models such as the complete Mindlin and Deresiewicz model should be addressed.

Keywords: DEM simulations; Granular flow; Contact force modeling

1. Introduction

The number of processes involving solids in the chemical, petrochemical, pharmaceutical, biochemical, food industry as well as in energy conversion and environmental processes is such that a high percentage of the research activity is concerned with solids. They appear as raw materials, products or intermediates at some stage in the process in a remarkable number of technological applications. Unfortunately, while the motion of gases and liquids is generally known to follow Navier–Stokes equations, the motion of solids presents different characteristics depending on the type of system, solid concentration and interactions, showing solid-like behavior when a packed bed is subjected to quasi-static stresses or liquid-like behavior, for example in fluidized beds, or a mixture of different behaviors with more complex rheological response. Although large sets of experimental data are available today on diverse granular and multi-phase flows, a proper discussion and understanding of the involved phenomena cannot be attained without the help of numerical simulations.

The computational tools developed in the last decades allow the analysis of the processes at a very small time and space scale and with no intrusion in the system. For fluid–solid flows, typically in fluidized beds, an approach is based on an Eulerian model of the system, the two-fluid model

* Corresponding author. Tel.: +39-0-984-496654; fax: +39-0-984-496655.

E-mail address: alberto.direnzo@unical.it (A. Di Renzo).

0009-2509/$ - see front matter © 2003 Elsevier Ltd. All rights reserved.
doi:10.1016/j.ces.2003.09.037

(TFM), where the fluid and the solids are considered as interpenetrating continuous phases (recent applications can be found in Peirano et al., 2002; Pain et al., 2002; Huilin et al., 2003). Also, numerical simulation examples using the TFM-based MFIX code (Syamlal et al., 1993) were carried out by McKeen and Pugsley (2003). The numerical computation is performed solving the averaged Navier–Stokes equations for both phases. Closure equations, related to the solid rheology and usually derived from the kinetic theory of gases, are necessary. The theoretical framework for this approach was established by Anderson and Jackson (1967).

Alternatively, a very promising technique appears to be the distinct element method (DEM) (Cundall and Strack, 1979). The basic idea behind the DEM is simple but very effective: the trajectory of each particle inside the system is calculated, considering all the forces acting on it and integrating Newton's second law of motion and the kinematic equations for position and orientation. The typical forces considered are: gravitation, contact forces due to collisions, solid–solid interactions such as electrostatic, Van der Waals, cohesive forces and bridging due to humidity or high-temperature operations and fluid–solid interactions in multiphase flows. Compared to the TFM, the DEM allows more fundamental studies on the system, in the sense that no hypotheses on the rheological behavior of the solid phase is needed, and especially detailed results in terms of microscopical properties can be obtained (Tsuji et al., 1998). These unsurpassed features are of paramount importance in order to understand the dynamics of mixing and segregating phenomena, agglomeration and flocculation, bubble formation, growth, coalescence and break-up in multi-phase systems, fixed to fluidized-bed transition for complex fluidized systems, basic mechanisms of dust formation and so on. Usual applications of the DEM have dealt with free flowing, i.e. non-cohesive, solids (Tsuji et al., 1992, 1993; Hoomans et al., 1996; Walton and Braun, 1986), although interesting applications in cohesive particle modeling exist in literature (Mikami et al., 1998; Rhodes et al., 2001; Nase et al., 2001; Moreno et al., 2003). When long-range inter-particle forces (e.g. Van der Waals, electrostatic, bridge formation forces) are negligible, the most important contribution to particle motion is due to collisions. They determine the direction of the motion of particles after the collision and, during the collision, the value of the force can be several orders of magnitude larger than the gravitational force, as will be discussed in the following sections.

In the field of granular motion simulations, two methodologies exist for particle–particle contact modeling: *hard-sphere* and *soft-sphere* approach. In the first case, single binary collisions are modeled as instantaneous processes and the properties of the particles after the collision are related to the properties of the particles before the collision through momentum and energy balances. Several examples of applications of the hard-sphere approach can be found in literature (Campbell and Brennen, 1984, and, more recently, Hoomans et al., 1996; Li and Kuipers, 2003). However, the binary collision concept restricts the application of the method to systems where multiple simultaneous collisions are unlikely to occur, i.e. to *dilute* systems. An additional drawback is inherent in the method, i.e. the impossibility to incorporate long-range inter-particle forces in the model (Xu and Yu, 1997). By adopting the *soft-sphere* approach, multi-particle collisions can be dealt with and these inter-particle forces easily implemented, at the cost of higher computational times. In fact, the force–velocity–displacement evolutions are simulated *during* the collision, modeling the contact as a mechanical system such as a linear spring–dashpot model or more a complex non-linear system.

DEM has been applied successfully in simulating and predicting the performances of many processes involving granular solids. A non-exhaustive list includes the work on hopper flow by Langston et al. (1995), the works on chute flow of glass spheres by Hanes and Walton (2000) and ellipsoidal particles (soybeans) by Vu-Quoc et al. (2000), the works on fluidization by Gera et al. (1998), Kafui et al. (2002), Kawaguchi et al. (1998, 2000), on fluidized beds with immersed tubes by Rong et al. (1999) and with lateral blasting by Xu et al. (2000), the works on solids motion in mills by Mishra and Murty (2001) and Venugopal and Rajamani (2001), the work on industrial granular flows by Cleary and Sawley (2002) and the work on an impact of a projectile on granular matter by Tanaka et al. (2002).

Although the most common contact force model is the linear spring–dashpot–slider system, more detailed contact force models, based on the classical Hertz's theory (Hertz, 1882) for the normal direction and on simplifications of the model developed by Mindlin and Deresiewicz (1953) for the tangential direction, have been used in the past (Tsuji et al., 1992; Vu-Quoc and Zhang, 1999). However, the problem of a comprehensive comparison of the simulation capabilities and an assessment of the suitability of these models for diverse DEM applications is still open, despite a few works are available in literature (e.g. Sadd et al., 1993). The aim of this work is to investigate the capabilities of three different contact models of describing the macroscopic and microscopic characteristics of a collision. Results obtained using a linear spring–dashpot–slider system, a simplified and a full Hertz–Mindlin and Deresiewicz models are compared on a macroscopic scale to experimental data provided by highly reproducible and accurate experiments on oblique elastic collisions of a sphere against a flat wall (Kharaz et al., 2001). Microscopically, the evolutions of fundamental properties of the particle are compared to an approximation, developed by Maw et al. (1976), of the elastic–frictional response of the system.

2. Mechanics of the frictional–elastic particle–wall oblique collision

Following the soft-sphere approach, the total contribution of simultaneous collisions is decomposed into the

single contributions of each particle–particle collision. Under certain assumptions (Maw et al., 1976), a particle–particle collision can be geometrically simplified into two symmetric collisions of the two particles with flat walls placed on the plane of the contact area. In particular, if the contact area is assumed to be circular and the traction components perpendicular to the direction of motion are neglected, then the instantaneous force–displacement relation for a particle colliding with another particle will be equal to the corresponding force–displacement relation for a collision of the particle with a wall. Therefore, an elementary collision of a particle against a flat wall is considered in this work as a case study for comparison.

Although in real collisions, a certain degree of dissipation is always present, due to microscopic plastic deformations and to friction between contacting surfaces, in the present work a frictional perfectly elastic collision will be examined. This idealized representation of the actual process provides the basis for models that take into account more complex phenomena. Also, well-established models for this problem are available in literature (Johnson, 1985). More realistic elasto-perfectly plastic models have also been developed (Thornton (1997) in normal direction and Vu-Quoc et al. (2001) in tangential direction). However, in the authors' opinion, they need more experimental validation, especially in tangential direction.

In DEM-based approaches, starting with the initial condition, the forces are related to the positions and velocities of the particles and Newton's second law of motion is integrated twice in order to find the new velocities and positions, so the cycle restarts. Therefore, the force–displacement calculation is performed in a displacement-driven manner, i.e. the forces depend on the actual displacements. The three contact force models examined differ in the functional relationship between these variables and/or in the different degree of approximation of the underlying phenomena.

In conventional DEM approaches, the normal and tangential displacements of a particle colliding with a wall are evaluated in terms of the actual position and orientation of the particle. Considering the two-dimensional problem of a particle approaching a horizontal flat wall (Fig. 1) with an initial translational velocity v_0, rotational velocity ω_0 and neglecting gravitational effects, the normal and tangential displacements in a generic instant during collision can be calculated with the following procedure. Even during the contact, the particle is assumed to maintain its spherical shape. As a consequence, the interpenetration, i.e. the difference between the radius of the particle R and the height of the particle center from the wall y, is a measure of the normal displacement δ_n:

$$\delta_n = R - y. \tag{1}$$

Analogously, the tangential displacement can be calculated considering the change in the position of the particle with respect to the initial position of impact, having subtracted the rolling contribution (Fig. 2). The calculation can be done

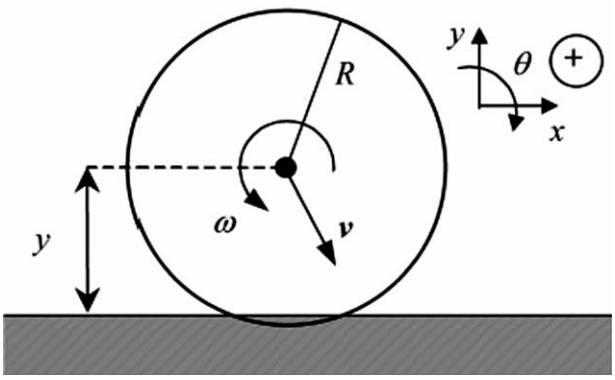

Fig. 1. Configuration for the contact problem.

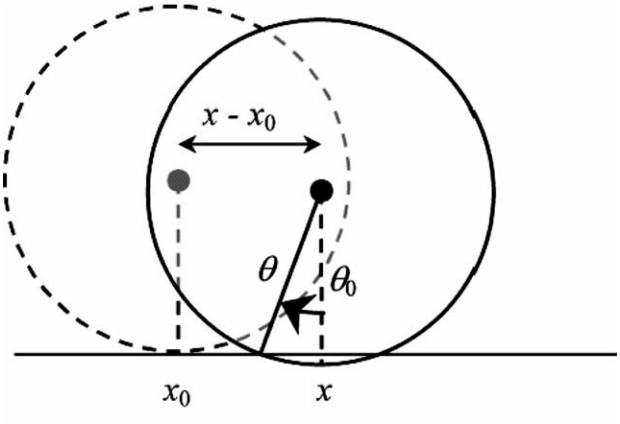

Fig. 2. Illustration of the tangential displacement.

in one step:

$$\delta_t = x - x_0 - [(\theta - \theta_0) \cdot (-R)]. \tag{2}$$

It is evident that the condition where the translational displacement of the particle $x - x_0$ equals the rotation at the contact point $(\theta - \theta_0) \cdot (-R)$ corresponds to *pure rolling* and the tangential displacement is zero. The definition of the contact model is necessary in order to formulate the normal and tangential force–displacement relations.

2.1. The theory of Hertz–Mindlin and Deresiewicz

The theory of frictional elasticity of a compliant sphere in contact with a wall was first developed by Hertz (1882) (also reported in Johnson, 1985) for the normal contact and by Mindlin and Deresiewicz (1953) for the tangential direction. Unfortunately, for a general oblique impact it is not possible to derive the direct tangential force–displacement relationship. However, a series of conditions was identified in the work of Mindlin and Deresiewicz (1953) who developed a set of rules for the generalization from simple cases to the oblique impact problem with an incremental procedure. Their work demonstrates that, due to the presence of tangential slip, the general force–displacement relation depends on

the whole loading history and on the instantaneous rate of change of the normal and tangential force or displacement. Starting with the simple cases, the proposed procedure for the treatment of the impact problem will be roughly reported in the following subparagraphs in a form viable for *distinct element simulations*. The paper of Mindlin and Deresiewicz indicated the set of rules necessary to treat certain types of load-displacement paths and it was recently reviewed in the work of Vu-Quoc and Zhang (1999). However, a modification of the reviewed procedure is presented here, where a clearer distinction of the cases is drawn for convenient inclusion in DEM codes, as will be pointed out later on. Following the displacement-driven formulation suggested by Cundall and Strack (1979) for DEM simulations, different paths for normal and tangential displacements can be identified.

2.1.1. Normal displacement varying, tangential displacement zero

When there is no tangential displacement, the impact is collinear and the evolution of the system can be described with a simple non-linear relation. Considering the solution of the elastic problem for the general case of two spheres with different properties, the maximum pressure $p_{\max}$, the radius of the contact area a and the total normal displacement δ_n can be derived (Johnson, 1985):

$$p_{\max} = \frac{3f_n}{2\pi a^2}, \tag{3}$$

$$a = \left(\frac{3R_{\text{eq}}}{4E_{\text{eq}}}\, f_n\right)^{1/3}, \tag{4}$$

$$\delta_n = \frac{a^2}{R_{\text{eq}}}, \tag{5}$$

whence the relation between the normal force f_n and the normal displacement is

$$f_n = -K_n \cdot \delta_n^{3/2}, \tag{6}$$

where the normal elastic constant results from the equivalent properties of the two materials as

$$K_n = \frac{4}{3}\, E_{\text{eq}} \sqrt{R_{\text{eq}}}. \tag{7}$$

The definitions of the parameters for two bodies of different materials, i.e. the equivalent Young's modulus E_{eq} and the equivalent radius R_{eq}, are reported in the appendix.

2.1.2. Normal displacement constant, tangential displacement varying

In a constant normal displacement case, the normal force and hence the radius of the contact area are constant. In these conditions, the tangential force during the cycle can always be related to the actual tangential displacement, provided that the loading path, e.g. first loading, unloading or reloading, is defined. However, since this is not true when the normal and tangential displacements vary simultaneously (subsequent paragraphs), an incremental procedure must be used in general, relating the change in tangential force to the change in tangential displacement. The actual tangential force f_t is calculated considering the previous tangential force f_{t0} and the change of the tangential displacement $\delta_t - \delta_{t0}$ through an incremental stiffness K_t:

$$f_t = f_{t0} + K_t(\delta_t - \delta_{t0}). \tag{8}$$

Using the incremental approach, the information regarding the loading history is stored in the previous tangential force and displacement. Therefore, if the tangential elastic constant K_t is properly calculated, the tangential force can be evaluated accurately. Considering the case where the normal displacement is held constant, when a tangential displacement is applied for the first time, the tangential stiffness can be calculated on the basis of the actual normal displacement

$$K_t = K_{t0}\left(1 - \frac{\frac{2}{3}K_{t0}\delta_t}{\mu f_n}\right)^{1/2}, \tag{9}$$

where μ is the friction coefficient. The initial stiffness constant K_{t0} is a function of the equivalent shear modulus and radius (see the appendix) and of the actual normal displacement

$$K_{t0} = 8G_{\text{eq}}\sqrt{R_{\text{eq}} \cdot \delta_n}. \tag{10}$$

Alternatively, since the force–displacement relation is unique, in terms of the actual normal force

$$K_t = K_{t0}\left(1 - \frac{f_t}{\mu f_n}\right)^{1/3}. \tag{11}$$

A complete first loading force–displacement path can be built through successive incremental steps. The shape of the tangential stiffness constant arises from the condition of micro-slip occurring between the contacting surfaces. A limit on the maximum tangential stress indeed exists as stated by Coulomb's law of friction

$$|t| \leqslant \mu |p|. \tag{12}$$

Eq. (12) must be satisfied throughout all the contact area. For a general constant normal displacement path, there is always a part of the contact area where Coulomb's law of friction is valid with the equal sign. This condition is often referred to as *micro-slip*. When the slip area covers the whole contact area, the condition is that of *gross sliding* and no adhering portions of the two surfaces exist. In this case, the law of friction is valid on an integral scale

$$|f_t| = \mu |f_n| \tag{13}$$

and the correspondent value of the stiffness constant tends to zero.

The unloading path is different from the loading path because of the presence of micro-slip between the contacting surfaces and a hysteretic behavior is observed. When the tangential displacement starts decreasing, the stress and local displacement distributions of the *turning point* must be accounted for in some way. Mindlin and Deresiewicz suggested that the turning force $f_t^{(TP)}$ should be used in the

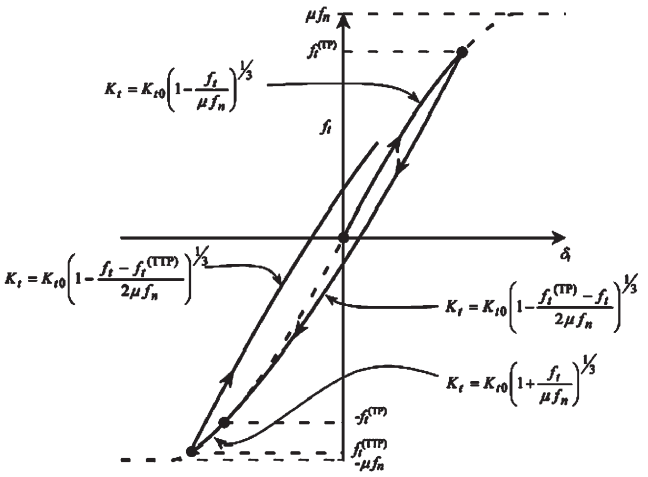

Fig. 3. Tangential elastic constants for the different branches of f_t–δ_t curve, for the case of constant normal displacement.

calculation of the stiffness constant. Consequently, during an unloading path, Eq. (8) is used in conjunction with the following elastic constant:

$$K_t = K_{t0}\left(1 - \frac{f_t^{(TP)} - f_t}{2\mu f_n}\right)^{1/3}. \tag{14}$$

An analogous formula can be derived in terms of the displacement at the turning point $\delta_t^{(TP)}$ but it will not be reported here. Following successive incremental constant-normal-displacement steps a complete unloading curve can be built, decreasing the tangential displacement until $-\delta_t^{(TP)}$. At that point, the stress and deformation distributions can be demonstrated to be equal to the case of negative first loading and all the previous positive loading history has no more influence.

After a second turning point $f_t^{(\mathrm{TTP})}$ is encountered (*reloading* path), the correspondent stiffness constant will be

$$K_t = K_{t0}\left(1 - \frac{f_t - f_t^{(\mathrm{TTP})}}{2\mu f_n}\right)^{1/3}. \tag{15}$$

An illustration of the typical *first loading–unloading–reloading* paths is showed in Fig. 3, together with the corresponding values of the tangential elastic constant K_t for each of the cases.

2.1.3. Normal displacement varying, tangential displacement varying

A set of rules is necessary in order to generalize the calculation reported in Section 2.1.2 to a case where the normal and tangential displacements vary simultaneously. The underlying idea is to build the constant normal displacement f_t–δ_t curves for the previous and the actual normal displacements and then to move from one curve to the other through a series of elementary steps. Under certain assumptions, the procedure can be demonstrated to be rigorous, but, unfortunately, the hypotheses are often not satisfied and the resulting calculation is approximated though still near the real solution. The basic assumptions are:

Assumption 1. Circular contact area and pressure distribution as prescribed by Hertz theory.

Assumption 2. The change in normal displacement and the change in tangential displacement are not interconnected, i.e. the problem can be solved by superposition of the two separate effects.

Assumption 3. Each incremental step starts from a *simple loading history* condition (see Definition 1).

Assumption 4. No torsion or rolling is taken into account.

Definition 1. The *simple loading history* condition is defined as the condition in which the state of the system $(\delta_n, \delta_t, f_n, f_t)$, independently of the loading path, can also be reached through a constant normal displacement (corresponding to δ_n) tangential loading curve f_t–δ_t (through a *first loading*/*unloading*/*reloading* path).

Consider the case of *increasing normal displacement* and *increasing tangential displacement*. Due to Assumption 1, the new normal force can be evaluated directly as described in Section 2.1.1. Therefore, the tangential problem can be solved with the aid of the tangential f_t–δ_t curves corresponding to the previous and the new constant normal displacements δ_{n0} and δ_{n1}, respectively (Fig. 4). Starting from the state **0** on the curve at previous constant normal displacement δ_{n0} (due to Assumption 3), it can be demonstrated that the tangential force–displacement relation follows a linear pattern up to state **1** with slope K_{t0} (Eq. (10)) evaluated at δ_{n1}. For displacements greater than δ_{t1} (e.g. δ_{t2} in Fig. 4) the tangential loading path follows the constant normal displacement curve for δ_{n1}, for example until state **2**.

As it is clear from Fig. 4, state **1** is located on the tangential curve corresponding to the new constant normal displacement δ_{n1}. As a result, this state defines the minimum tangential displacement change $\Delta\delta_t$ in order to maintain the simple loading history assumption (Assumption 3) valid for the next step. It shall be noted that the change of the tangential force is equal to $\mu\Delta f_n$, indeed often Assumption 3 is stated in terms of change of tangential force with respect to change of normal force as

$$|\Delta f_t| \geqslant \mu|\Delta f_n|. \tag{16}$$

Alternatively, in terms of the changes of displacement

$$|\Delta\delta_t| \geqslant \Delta\delta_t^{(SL)} = \frac{\mu|\Delta f_n|}{K_{t0}}, \tag{17}$$

where $\Delta\delta_t^{(SL)}$ is the minimum change of tangential displacement in order to preserve the *simple loading history* condition, which in this case is $\Delta\delta_t^{(SL)} = \delta_{t1} - \delta_{t0}$. K_{t0} is evaluated at the new normal force f_{n1}.

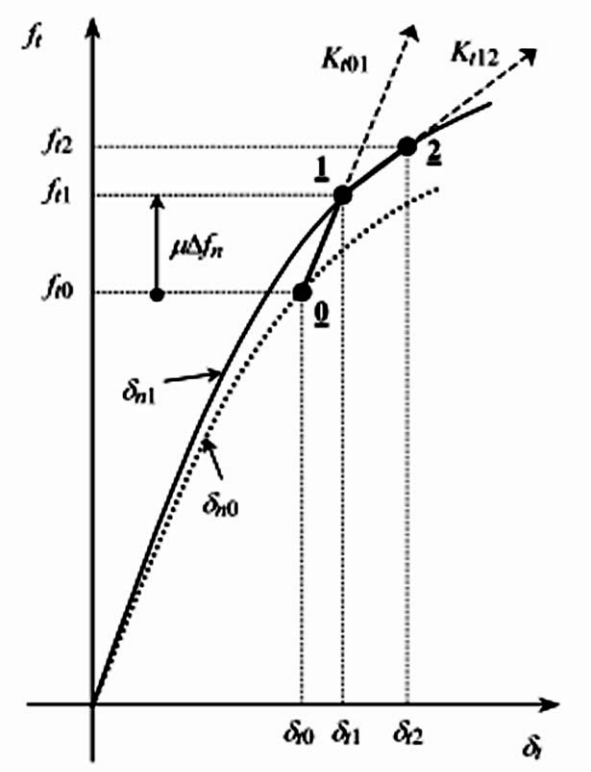

Fig. 4. Tangential loading path for the case: increasing δ_n, increasing δ_t. The calculation of the total transformation **0**–**2** is split into two constant normal displacement steps: **0**–**1** and **1**–**2**. The two f_t–δ_t curves correspond to the previous (dotted line) and the new (solid line) constant normal displacement δ_n.

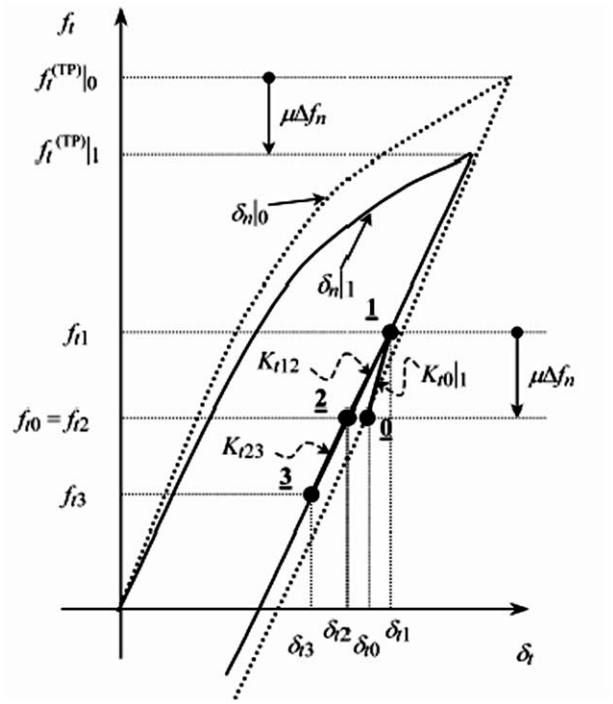

Fig. 5. Tangential loading path for the case: decreasing δ_n, decreasing δ_t. The calculation of the total transformation **0**–**3** is split into three constant normal displacement steps: **0**–**1** **1**–**2** and **2**–**3**. The two f_t–δ_t curves correspond to the previous (dotted line) and the new (solid line) constant normal displacement δ_n.

The state change from the initial state **0** to the actual state determines whether ($\delta_t \geqslant \delta_{t1}$) or not ($\delta_t < \delta_{t1}$) the subsequent steps will satisfy Assumption 3.

From a computational point of view, state **1** is characterized by the following tangential force and displacement:

$$f_{t1} = f_{t0} + \mu\Delta f_n, \tag{18}$$

$$\delta_{t1} = \delta_{t0} + \Delta\delta_t^{(SL)}. \tag{19}$$

This allows the final state of the system to be easily calculated depending upon the relative change of the tangential displacement. If δ_t is less than δ_{t1} (no *simple loading history* following) the new force f_t can be calculated as

$$f_t = f_{t0} + K_{t0}|_1 \cdot (\delta_t - \delta_{t0}). \tag{20}$$

Otherwise (*simple loading history* following), a two-step calculation is required. State **1** is first reached through Eq. (18) and then the second step (to state **2** in Fig. 4) is carried out along the new constant normal displacement curve, through a stiffness constant K_{t12} calculated at state **1**:

$$K_{t12} = K_{t0}|_1 \left(1 - \frac{f_{t1}}{\mu f_{n1}}\right)^{1/3}, \tag{21}$$

$$f_{t2} = f_{t1} + K_{t12} \cdot (\delta_{t2} - \delta_{t1}). \tag{22}$$

As it is presented, this derivation is valid for a *first loading* case (Fig. 4). However, the procedure can be easily generalized also to *unloading* and *reloading* cases for normal displacement increasing and decreasing. In order to describe the fundamental concepts at the basis of the procedure the case of *normal displacement decreasing* and *tangential displacement decreasing* will be shortly described (Fig. 5).

All the cases where the normal displacement decreases do not have problems regarding the *simple loading history* hypothesis. The final state of the mechanical transformation always lays on the new constant normal displacement curve, hence the *simple loading history* condition is satisfied, provided that in all the previous steps simple loading paths were followed.

The full transformation is subdivided into elementary steps. State **1** is reached along a straight line of slope $K_{t0}|_1$, so that the corresponding force increases ($\Delta f_n < 0$):

$$f_{t1} = f_{t0} - \mu\Delta f_n. \tag{23}$$

Since the tangential displacement decreases (*unloading* curve) the final state will be on the lower part of the unloading part of the constant normal displacement curve. In order to take the subsequent step from state **1** to the new state (e.g. state **3** in Fig. 5), the stiffness constant K_{t13} is necessary. It can be calculated directly corresponding to

state **1** (using Eq. (14)):

$$K_{t13} = K_{t0}|1\left(1 - \frac{f_t^{(TP)}|_1 - f_{t1}}{2\mu f_n}\right)^{1/3}, \tag{24}$$

where $f_t^{(TP)}|_1$ is the turning point force updated because of the change in the normal displacement. This update is

$$f_t^{(TP)}|_1 = f_t^{(TP)}|_0 + \mu\Delta f_n \tag{25}$$

and is valid for all the changes in normal displacement.

The final force at state **3** can then be calculated as

$$f_{t3} = f_{t1} + K_{t13}\cdot(\delta_{t3} - \delta_{t1}). \tag{26}$$

Alternatively, with better accuracy for large change of tangential displacement, the stiffness constant can be evaluated at state **1** and used to calculate the displacement δ_{t2}. Then another stiffness constant can be evaluated at state **2** (where the tangential force is equal to the previous step ($f_{t2} = f_{t0}$) and used to perform the last step from states **2** to **3**.

All the remaining cases, including all the cases near the turning points, can be treated in the same manner, paying attention to the subdivision into elementary steps and the corresponding stiffness constant evaluations. Other discussions of the procedure of Mindlin and Deresiewicz exist in literature such as the very clear presentation that can be found in Vu-Quoc and Zhang (1999). However, it shall be noted that, compared to other reviews of the solution of the tangential elastic–frictional problem, the procedure reported in the present work is truly displacement driven. The main difference is that the selection of the cases (normal and tangential increases or decreases) is based upon the displacements and not upon the forces. This is particularly important because the change in tangential force cannot be defined before the calculation is carried out and the calculation depends upon the case, i.e. the change in tangential force. Instead, in granular flow simulation with the DEM the tangential displacement is available at the beginning of the calculation process (see Section 2); therefore, the selection must be based on the displacement itself, otherwise the procedure is inconsistent.

2.2. The Maw, Barber and Fawcett (MBF) solution

The description of the micromechanics of contacting spheres presented by Mindlin and Deresiewicz (1953) is very important for understanding the evolution of the forces and displacements during impacts. However, the assumptions at the basis of the theory are not always valid in elastic impact problems, as will be illustrated in the results of the comparison (Section 4). A more rigorous approach was proposed in the work of Maw et al. (1976), where discretization of the space domain (the contact area) was implemented as well as time discretization. A brief summary of the method will be presented here.

The contact area is subdivided into a number of concentric annuli, where the normal and tangential traction distributions and the displacements are evaluated at each time-step. At the foundations of the mechanical model only Assumptions 1 and 2 of Section 2.1 are considered. Non-axisymmetric terms are neglected, giving rise to a circular contact area and the normal and tangential problems are solved independently. No assumptions regarding the loading history is made in the mathematical development.

A resulting set of linear equations, one for each annulus, is solved for each time step during the collision. Different shape equations result from the tangential problem depending upon the state of the annulus considered. For sticking annuli the results of the elastic theory are used, whereas for slipping annuli the Coulomb's law of friction on a microscopic basis is applied.

Analogous to the theory of Hertz–Mindlin and Deresiewicz, the approximated analytical results will be reported here in a general form suitable also for collision between bodies with different material properties. The normal problem leads to the following relation for the force (Eq. (4) rearranged):

$$f_n = \frac{4E_{\mathrm{eq}}}{3R_{\mathrm{eq}}}a^3, \tag{27}$$

where the actual radius of the contact area a is related to the normal displacement (Eq. (5)) or, in the notation of the method, the normal displacement of the central annulus. Another interesting result reported by Maw et al. (1976) is the computation of the collision duration as a function of the normal component of the impact velocity, v_{n0}:

$$\tau_c = \frac{4\Gamma\left(\frac{2}{5}\right)\sqrt{\pi}C^2R_{\mathrm{eq}}}{5\Gamma\left(\frac{9}{10}\right)v_{n0}}, \tag{28}$$

where $\Gamma(\cdot)$ is the gamma function. The definition of this characteristic time, as in Eq. (28), is valid only for collisions of a particle with a wall.

The maximum radius of the contact area $a^{(\max)}$ can also be calculated a priori as

$$a^{(\max)} = C\cdot R_{\mathrm{eq}}. \tag{29}$$

The constant C in Eqs. (28) and (29) is another function of the impact velocity, the equivalent mass M_{eq} and the material properties of the solids

$$C = \left[\frac{15M_{\mathrm{eq}}v_{n0}^2}{16E_{\mathrm{eq}}R_{\mathrm{eq}}^3}\right]^{1/5}. \tag{30}$$

In the tangential direction, the problem is formulated describing the tangential stress at a certain radius r as a summation of contributions multiplied by coefficients w_i:

$$t(r) = \sum_{i=j}^{n} w_i\sqrt{1 - \frac{r^2}{(a^{(\max)}\cdot i/n)^2}}, \tag{31}$$

where j is the smallest integer greater than $n\cdot r/a^{(\max)}$.

Equations are solved for each of the coefficients w_i depending upon sticking or slipping conditions. From them,

the total tangential force can be evaluated directly as

$$f_t = \frac{2\pi(a^{(\max)})^2}{3} \sum_{i=1}^{n} \frac{i^2}{n^2} w_i. \tag{32}$$

The global tangential displacement δ_t is always considered as the displacement measured at the innermost annulus. In order to gain greater generality the results are presented in non-dimensional terms. Two parameters are needed in order to characterize the system: the non-dimensional tangential velocity of the contact point ψ and a combination of geometrical, physical and mechanical properties χ:

$$\psi = \frac{\kappa}{\mu} \frac{v_t}{v_{n0}}, \tag{33}$$

$$\chi = \frac{\kappa(1 + 1/R_g^2)}{2} \tag{34}$$

where v_t is the tangential velocity of the contact point, $R_g = \sqrt{I/MR^2}$ is the non-dimensional radius of gyration and I is the moment of inertia of the sphere. κ is a combination of the material properties of the bodies and corresponds to the initial tangential to normal stiffness constant ratio (for the definition see the appendix). It shall be noted that in Eq. (33) the non-dimensional tangential velocity ψ is a function of the *initial* normal velocity v_{n0}. Therefore, the initial value of ψ, ψ_0, for definite material properties, is proportional to the impact angle of a non-rotating sphere. This is why ψ_0 is often referred to as the non-dimensional angle of incidence.

The non-dimensional results can be summarized in terms of these two parameters:

(1) $\psi_0 < 1$: The impact starts with surfaces sticking until the midpoint is reached. Then the contact area starts shrinking and an outer annulus of micro-slip spreads inwards until, during the last part of the collision, the whole contact area slides (gross sliding).
(2) $1 < \psi_0 < 4\chi - 1$: the impact starts in gross sliding condition but, at some point, sticking occurs almost instantaneously, due to changes in tangential and normal forces. The rest of the impact continues as in case (1), with a final part of gross sliding.
(3) $\psi_0 > 4\chi - 1$: the impact takes place entirely in gross sliding.

3. Description of the compared models

Although the solution procedure MBF is rigorous and accurate, it is also extremely time consuming for *distinct element simulations*. Apart from considerations of computational time for large numbers of particles (10^5–10^6), there is also another important issue to consider. The computational effort required for a very accurate model may not be worth it because it is based on geometrically ideal particles, whereas no perfectly smooth spheres are found in practical applications. The intention of the comparison is to evaluate the capabilities offered by simplified models and to derive indications on what is the most appropriate model for the different applications. Three models have been selected for comparison: a linear model, a simplified no-slip (H–MDns) and a full Hertz–Mindlin and Deresiewicz (H–MD) model. Other models, based on different degrees of simplification, can be found in literature (e.g. Walton and Braun, 1986; Thornton and Yin, 1991; Vu-Quoc and Zhang, 1999) but are not included in the analysis since they can be considered at an intermediate complexity between linear H–MDns and H–MD.

3.1. The linear model

The most intuitive and simple way of modeling mechanical relations is to use combinations of linear mechanical elements in series or parallel in order to represent the dynamical system with the appropriate characteristics. This was the idea of Cundall and Strack (1979), who proposed a parallel linear spring–dashpot model for the normal direction and a parallel linear spring–dashpot in series with a slider for the tangential direction. The spring is placed for the elastic contribution to the response while the dashpot accounts for the dissipation due to plastic deformations. In this comparison, only frictional–elastic collisions are considered, thus the material parameters for the definition of the model are the normal and tangential spring constants (or elastic constants) K_n and K_t and the friction coefficient μ. They appear in the force–displacement relations for the normal and tangential force calculations:

$$f_n = -K_n \cdot \delta_n, \tag{35}$$

$$f_t = -\min(K_t \cdot |\delta_t|; \mu|f_n|) \frac{\delta_t}{|\delta_t|}. \tag{36}$$

The dissipation due to plastic deformations can be modeled using either a velocity dependent damping (e.g. Cundall and Strack, 1979) or an unloading spring with a different elastic constant (e.g. Walton and Braun, 1986). The latter approach is preferable because plasticity is a phenomenon related to displacements and not to velocity. The respective parameters are usually derived from the coefficient of restitution.

3.2. The H–MDns model

A more accurate mathematical representation of the physical problem can be obtained considering the model used by Tsuji et al. (1992). In the cited work, the authors for the first time introduced a non-linear model inside a multi-particle DEM code aiming at a proper simulation of the granular flow. The model uses the elastic theory of Hertz for the normal contact problem and the *no-slip* solution of the tangential contact problem as solved by Mindlin and Deresiewicz (whence the name *H–MDns*). Mathematically, the normal force is evaluated using Eq. (6), where the elastic constant is a function of the geometrical and physical properties of

the particle and wall as in Eq. (7) and the tangential force is evaluated without considering micro-slip phenomena:

$$f_t = K_{t0}\delta_t, \tag{37}$$

where K_{t0} calculated as in Eq. (10). It should be noted that the tangential force–displacement relation is linear, but the tangential elastic constant depends upon the normal displacement, correctly accounting for the different tangential behavior for different normal displacement states.

Although micro-slip is neglected, the gross sliding condition provided by Coulomb's law of friction is imposed as a constraint to the tangential force calculation.

3.3. The H–MD model

The complete theory of Hertz for the normal contact and Mindlin and Deresiewicz for the tangential problem is chosen for comparison as the more detailed model to use for collision simulations. The force–displacement relation is accurately modeled in all aspects examined by the theory of Mindlin and Deresiewicz. The influence of micro-slip on the microscopical tangential interactions has been discussed in Section 2.1 with all the implications regarding the non-linear tangential force–displacement relation and the hysteretic behavior for oscillating conditions. The algorithm to implement inside DEM codes is fairly complex in order to include all the possible combinations of normal and tangential displacement variations. However, since all *micro-slip* effects are correctly accounted for, a better simulation of oblique impacts is expected by the H–MD model. Mathematically, the normal problem is solved through Eqs. (6) and (7) and for the tangential problem all the combinations of the change of displacements are contemplated on the basis of the procedure indicated in Section 2.1.

4. Simulation results

The solutions of the frictional–elastic oblique impact of a sphere against a flat wall using the different models are to be compared on different scales. Microscopically, experimental measurements of the evolution of forces and displacements during collision are not available. Hence, on this scale, the results of the three models (linear, H–MDns and H–MD) are compared with the MBF solution. Since the basic assumptions of this approach are less restrictive than those necessary for the other three models (in particular, no assumptions regarding the loading history is necessary), and since the space discretization has been operated by using a large number of annuli ($n = 1000$), the approximated MBF solution is expected to be the most accurate and will be considered as "exact" in the following sections.

On a macroscopic scale, the results are compared with the experiments run by Kharaz et al. (2001). These authors also reported an excellent agreement between the experimental results and those obtained by Maw et al. (1976) under similar conditions ($\chi = 1.50$ in the experiments and $\chi = 1.44$ in the approximated analytical solution).

4.1. Simulation data

In this work, the data for the simulations are taken as those used in the experiments of Kharaz et al. (2001). A 5-mm-diameter aluminum oxide ($\rho = 4000$ kg m^{-3}) sphere impacting at a constant absolute velocity of 3.9 m s^{-1} against a thick soda-lime glass anvil is considered. The impact angle α was varied by rotating the anvil. The mechanical properties of the two materials taken from the work of Kharaz et al. (2001) seem to be inconsistent. The shear modulus G obtained by the Young's modulus E and the Poisson ratio v differs from the one reported in the material properties. Therefore, in this work a different consistent Young's modulus is calculated from the shear modulus G and the Poisson coefficient v as $E = 380$ GPa instead of $E = 360$ GPa. This modification, necessary for coherency, does not influence the characteristic properties of the system: the parameter κ, accounting for the material properties, changes correspondingly of only 0.01%.

These mechanical properties, listed in the last column of Table 1, can be directly used in the non-linear models H–MDns and H–MD. However, for the linear model a few assumptions are necessary in order to select the input parameters and the related problems will be discussed in Section 4.4. The normal and tangential elastic constants, K_n and K_t, must be related to the real mechanical properties. The linear parameters can be obtained from the non-linear f–δ relations, taking the derivative of the forces with respect to the corresponding displacements, calculated at a certain normal displacement. In this case, the point where to take this derivative must be chosen with some criterion. For example, if a typical maximum impact velocity can be estimated, the corresponding force $f_n^{(\max)}$ and displacement $\delta_n^{(\max)}$ can

Table 1
Mechanical properties

Aluminium oxide (particle)	Linear model	H–MDns/H–MD models
Normal elastic constants K_n (N m^{-1})	1.72×10^7	—
Tangential elastic constant K_t (N m^{-1})	1.48×10^7	—
Young's modulus E (GPa)	—	380
Poisson ratio v	—	0.23
Shear modulus G (GPa)	—	154
Friction coefficient μ	9.2×10^{-2}	9.2×10^{-2}
Soda-lime glass (wall)		
Normal elastic constants K_n (N m^{-1})	1.72×10^7	—
Tangential elastic constant K_t (N m^{-1})	1.48×10^7	—
Young's modulus E (GPa)	—	70
Poisson ratio v	—	0.25
Shear modulus G (GPa)	—	28
Friction coefficient μ	9.2×10^{-2}	9.2×10^{-2}

be calculated with the non-linear model. Then, the actual K_n can be set to the derivative $\mathrm{d}f_n/\mathrm{d}\delta_n$ calculated in $\delta_n^{(\max)}/2$ or simply to the slope $f_n^{(\max)}/\delta_n^{(\max)}$. However, sometimes it is difficult to estimate the typical velocities attained by particles in granular flow. Following the algorithm of Maw et al. (1976) and using the data of the experiments for a collinear collision with the wall, the elastic constant is calculated here as mentioned above. In particular, the values calculated using in sequence Eqs. (29), (27) and (5), respectively, are

$$a^{(\max)} = 2.1 \times 10^{-4}\ \text{m(max. radius of the contact area)},$$

$$f_n^{(\max)} = 293\ \text{N} \quad \text{(max. normal force)},$$

$$\delta_n^{(\max)} = 1.7 \times 10^{-5}\ \text{m(max. normal displacement)},$$

$$K_n = f_n^{(\max)}/\delta_n^{(\max)} = 1.72 \times 10^{7}\ \text{N m}^{-1}$$

The other important parameter is the tangential elastic constant. It can be simply assumed equal to the normal constant or, alternatively, when the mechanical properties of the particle are available, the tangential to normal spring constant ratio κ can be used to calculate K_t. In this work, in order to maintain coherency among the models, the same value of κ is used also in the linear model in order to evaluate K_t as a function of K_n. The friction coefficient μ is set to the value reported in the experimental work. The mechanical parameters used in the simulations are summarized in Table 1.

The numerical method for the integration of the equation of motion is the Euler method, as in Maw et al. (1976). More accurate integration schemes can be used, but the absolute accuracy is guaranteed here because the time-step is set to 1×10^{-8} s, so that more than 1000 steps are required for the simulation of the collision.

4.2. Macroscopic results compared with experiments

The simulated state variables, at the end of the collision, can be compared to the corresponding values obtained in equivalent experiments (Kharaz et al., 2001). Physical significance of the models is only ensured if all the properties calculated by the simulations match the actual observed values. Looking at the results available in the experimental work on elastic collisions, the simulated tangential coefficient of restitution can be plotted against the angle of incidence α (Fig. 6), defined with respect to the perpendicular to the wall. The plot shows very good agreement of the three models except for small angles.

In order to understand the reasons for this discrepancy, the underlying phenomena must be examined. As described in Section 2.2, for these angles, the global force–displacement relation is mostly due to microscopic tangential elastic contributions, the remainder being due to micro-slip. Only for small time intervals during the collision gross sliding is observed, usually at the beginning or at the end. Increasing the angle of impact, gross sliding occurs for a larger period until, for angles greater than a critical value α_c, all the impact occurs in gross sliding condition. The critical angle, for the system examined, can be calculated by the MBF solution, giving $\alpha_c \approx 28°$. When small tangential displacements are observed, the elastic mechanism dominates the evolution of the collision because small frictional effects occurs only at the end of the process. Only the elastic part of the theory is different among the models so that, for high impact angles ($\alpha > \alpha_c$), when the frictional mechanism dominates, all the models converge to the correct solution and reproduce the actual behavior very accurately. It is curious that, for small impact angles, the linear model predicts the tangential coefficient of restitution better than the non-linear H–MDns model. The only differences between the linear and H–MDns models are the functional variation of the normal load and the variation of the tangential spring constant with varying normal load. Evidently, neglecting micro-slip effects in the H–MDns model is worse than considering a constant tangential stiffness as in the linear model.

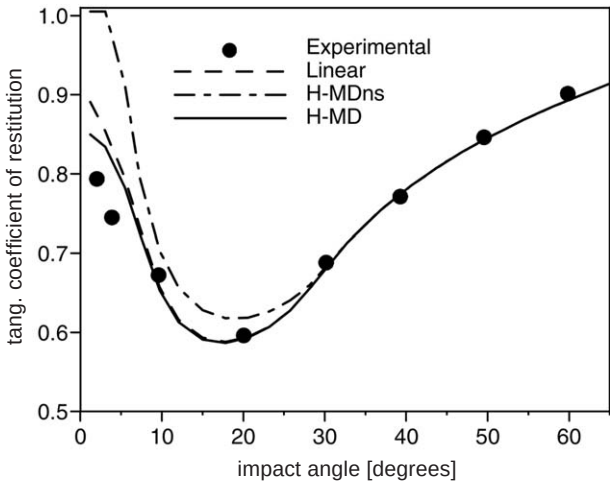

Fig. 6. Simulated and experimental tangential coefficient of restitution vs. impact angle.

In Fig. 7, the rebound angles of the contact point (a) and the center of mass (b) are plotted against the impact angle. The tangent of the rebound angle is equal to the tangential to normal velocity ratio at the moment of the particle detachment. The simulated curves match the experimental values with excellent agreement, confirming the capability of all the models to reproduce the correct global motion of the colliding particle, despite the differences in the underlying equations.

A further indication is given in Fig. 8, where the rotational velocity at the end of the impact is plotted for various impact angles. All the models predict values in excellent agreement with observation in the experiments. Slight differences occur for angles $\alpha < \alpha_c$ but a negligible effect is noted compared to experiments.

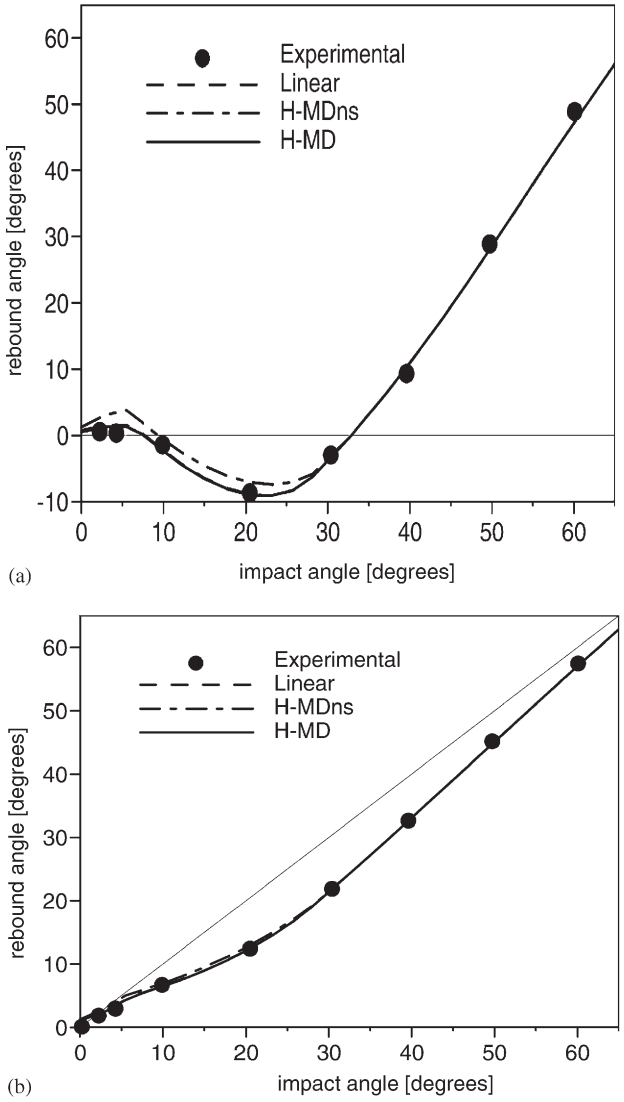

Fig. 7. Simulated and experimental rebound angles of the contact point (a) and the center of mass (b) vs. impact angle.

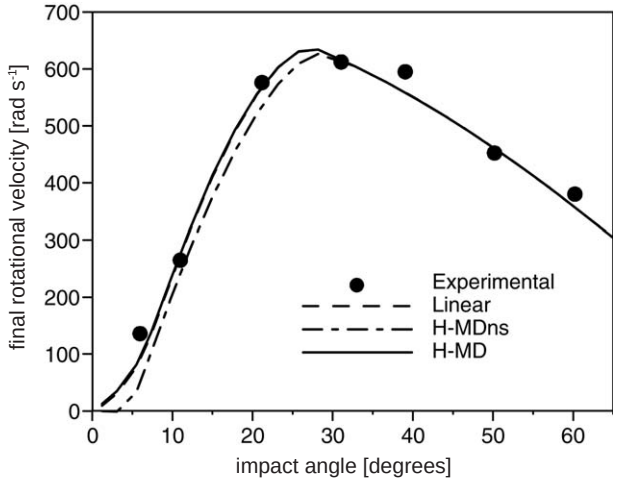

Fig. 8. Simulated and experimental rotational velocity at the end of the impact vs. impact angle.

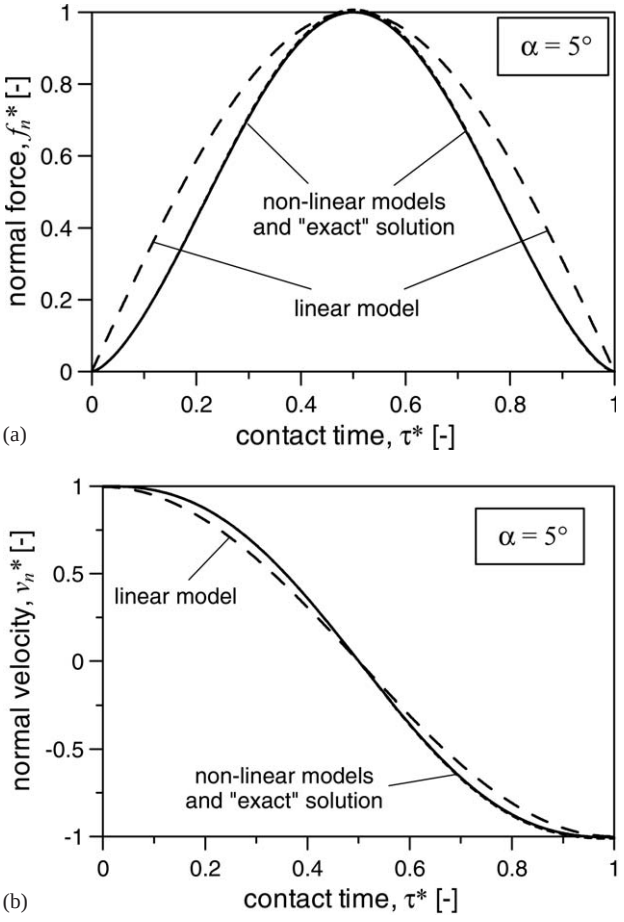

Fig. 9. Evolution of the normal force (a) and velocity (b) during an impact at 5°.

The comparison of the data observed and simulated using the force–displacement models brings to light a very good representation of the particle behavior during a collision, validating the numerical simulation on a physical basis in terms of the main process properties. However, it shall be pointed out that no time-related effects appear in the analysis. Indeed, nothing is said regarding the time scale of the process itself and the evolution of the variables involved. Characteristic velocities at the end of the process are compared starting with equal initial conditions. Therefore, more detailed analyses are necessary before general conclusions can be drawn.

4.3. Force–displacement microscopic results

On a microscopic basis, the models and the MBF "exact" solution can be compared for each time instant, evaluating the difference in the evolution of the normal and tangential forces, velocities and displacements. However, the duration of the impact modeled with a linear spring is different from that with non-linear relations. For the linear model,

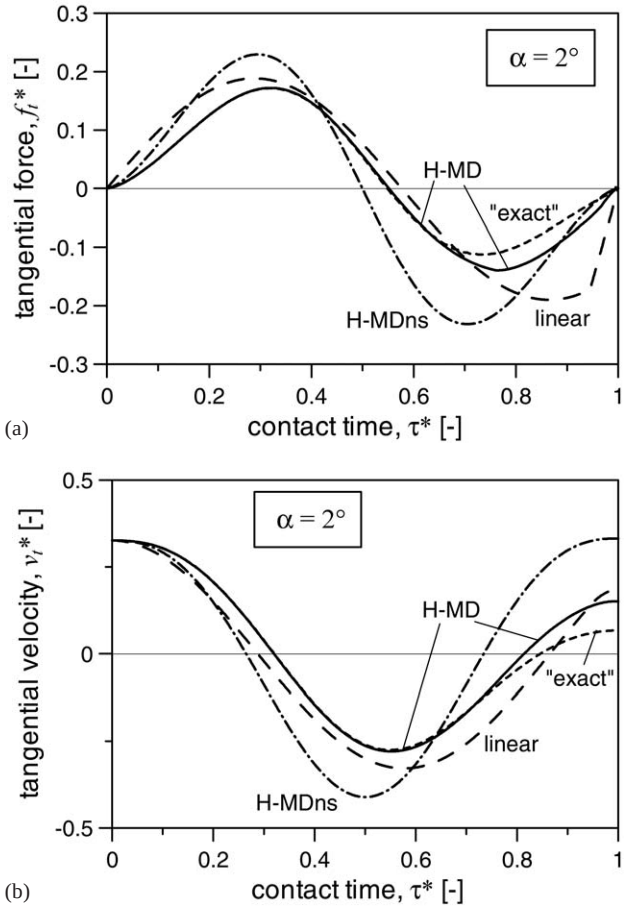

Fig. 10. Evolution of the tangential force (a) and velocity (b) during an impact at 2°.

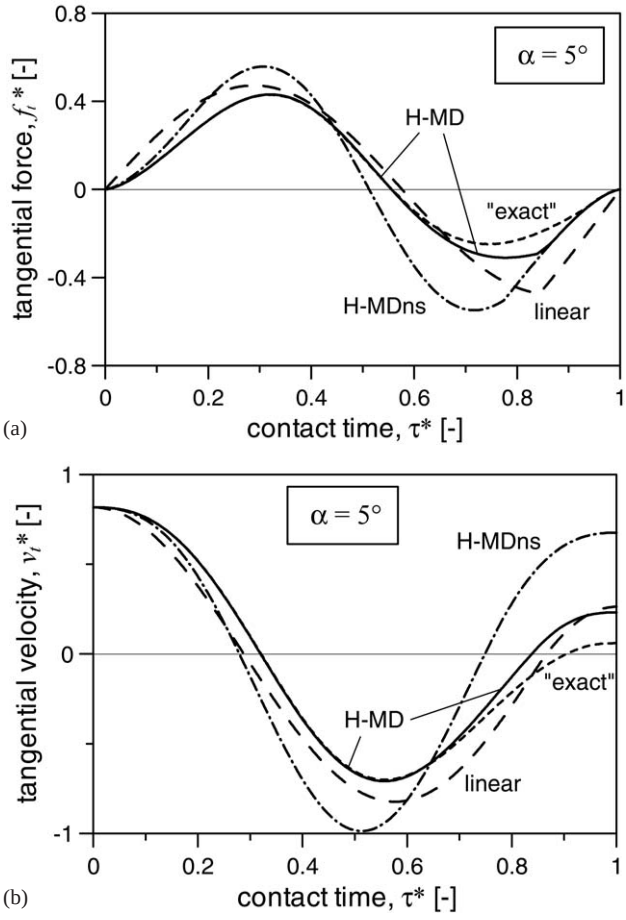

Fig. 11. Evolution of the tangential force (a) and velocity (b) during an impact at 5°.

it is a function of the particle density, diameter and elastic constant. In fact, the collision duration is half the oscillation period of the corresponding spring-mass system. For non-linear models, Eq. (28) describes the dependency of the collision time also on the impact velocity. Therefore, it can be showed that using non-linear models low-velocity impacts last longer than high-velocity ones, whereas with a linear model all the impacts have the same duration. In order to overcome the difficulties in plotting different time scales for the comparison, a non-dimensional time is taken as the independent variable. Analogously, also forces, velocities and displacements are expressed in non-dimensional form, following the procedure of Maw et al. (1976) (see the appendix).

The response of the system in normal direction is relatively simple. The evolution of the normal force during the collision for the non-linear (Hertz-based) models is indistinguishable from the "exact" solution (Fig. 9a for $\alpha = 5°$ inclined impact). Instead, the linear model differs in the initial and final slopes due to the different functional f–δ relation. The normal velocity profile calculated using the linear model follows quite accurately the profiles obtained using the non-linear and "exact" models (Fig. 9b). Similar results are obtained for different impact angles because no influence of tangential phenomena in normal direction is accounted for, therefore results for the normal properties for other impact angles will be omitted.

A different behavior is observed in tangential direction depending on the initial impact angle, because diverse microscopic mechanisms are involved. For almost collinear collisions ($\alpha = 2°$), the evolution of the tangential force during the collision shows clear differences among models (Fig. 10a). The linear model generally predicts a tangential force evolution in fairly good agreement with that of the "exact" solution, although, in the last part, a clear discrepancy can be observed. It is important to note that, as in the normal direction, the linear model line starts and ends with a non-zero slope. The H–MDns model shows a peculiar central symmetric behavior with respect to half of the impact duration. It quantitatively overestimates in modulus the extreme points, i.e. the maximum and minimum tangential force. The results of the complex H–MD model are superposed to the "exact" solution for most of the collision duration, although, towards the end of the process, a different curve is followed and the modulus of the minimum force is slightly overestimated. This difference is due to the

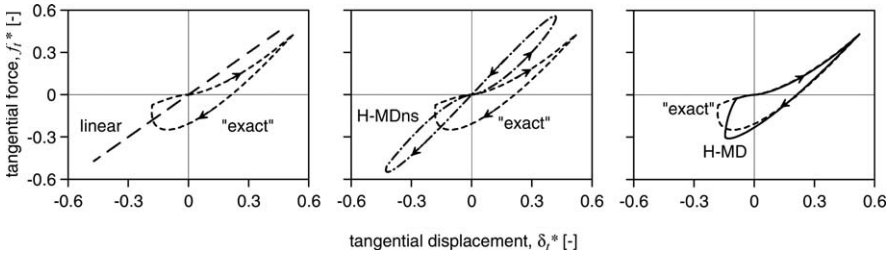

Fig. 12. Tangential force–displacement plot during an impact at 5°.

assumption of *simple loading history* at the beginning of each incremental step (Assumption 3) in the model developed by Mindlin and Deresiewicz, which is not valid when many *non-simple loading* steps have been carried out, or, in other words, at the end of the impact. Nevertheless, considering the differences obtained with simple models, the H–MD model can be considered very accurate.

The evolution of the tangential velocity (Fig. 10b) is fairly well approximated by the linear and H–MD models. It is worth noticing that the linear model predicts an evolution of the tangential velocity closer to the "exact" solution than the H–MDns model. With the latter, again symmetrical, larger (in modulus) minimum and final tangential velocity are calculated. For the H–MD model, the difference of the tangential force in the final instants ($\tau^* > 0.8$) is also reflected in the tangential velocity (Fig. 10b). Except this part, the velocity profiles obtained with the H–MD model and the "exact" solution are superposed. The tangential velocity v_t^*, as defined in the appendix, at the end of the contact can also be seen as a non-dimensional rebound angle. The comparison of the last values of v_t^* is, therefore, an enlargement of the experimental comparison reported in Fig. 7a, but it also provides a way to explore how the models approach that final value.

The results of the comparison for the collision at $\alpha = 5°$ are qualitatively similar to the previous case, as showed in Fig. 11. However, an increasing percentage of the impact occurs in gross sliding, as emphasized by the last instants of the collision. In order to better represent the loading–unloading–reloading path, an f_t–δ_t plot is showed in Fig. 12, comparing the three models with the "exact" procedure. This type of diagram clearly shows the effects of the increasing agreement of the models going from the linear to the H–MD model, although the H–MDns model seems to follow an unusual path. Both the linear and H–MDns models strongly overestimate the minimum tangential displacement and force.

An oblique collision at $\alpha = 10°$ shows both an initial and final part of the process occurring in gross sliding. It is indeed evident in Fig. 13a that an identical tangential force is obtained by the non-linear models at the beginning as well as at the end of the impact. The linear model differs from them due to its normal force profile, which directly influences the gross sliding tangential force profile. The H–MDns

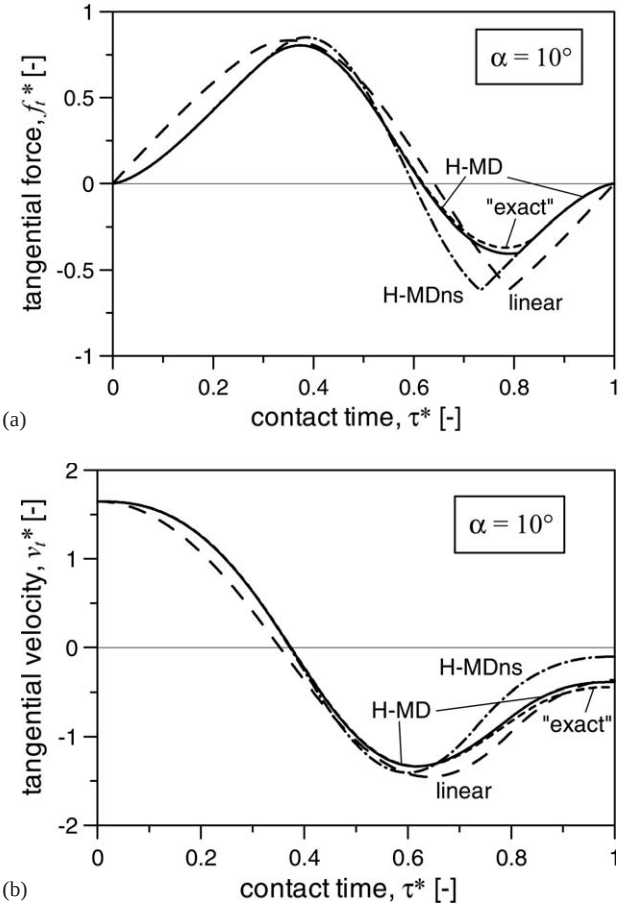

Fig. 13. Evolution of the tangential force (a) and velocity (b) during an impact at 10°.

model gives good results, because the main differences with respect to the complete H–MD model are limited to the intermediate part, where micro-slip effects, neglected in the H–MDns model, are predominant. Only a slight discrepancy remains between the H–MD and the "exact" model because the gross sliding at the end of the contact process leads to generally similar results from the models. The agreement with the MBF model for the tangential velocity predicted by the linear and H–MD models and the "exact" solution is fairly good during all the collision (Fig. 13b), whereas the H–MDns model shows major discrepancies for $\tau^* > 0.6$.

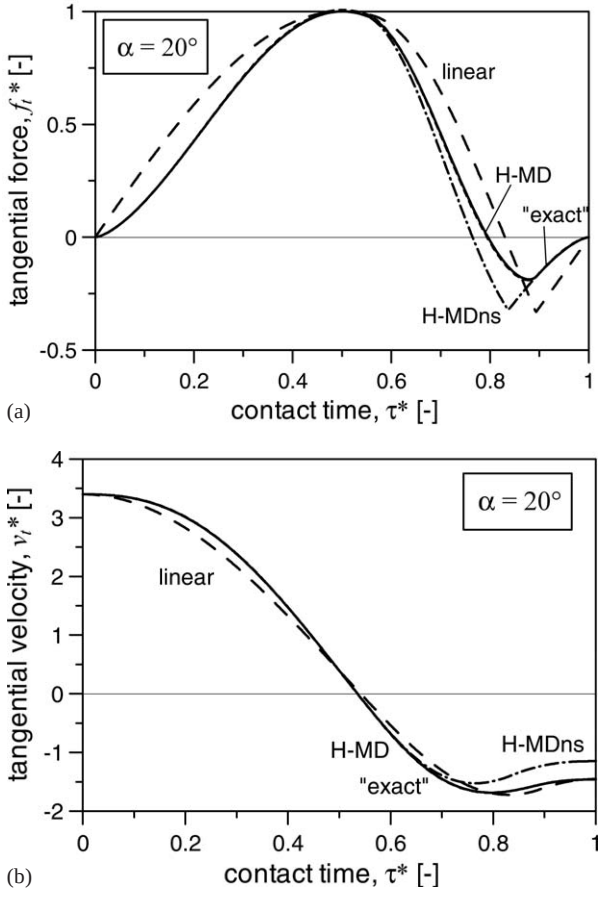

Fig. 14. Evolution of the tangential force (a) and velocity (b) during an impact at 20°.

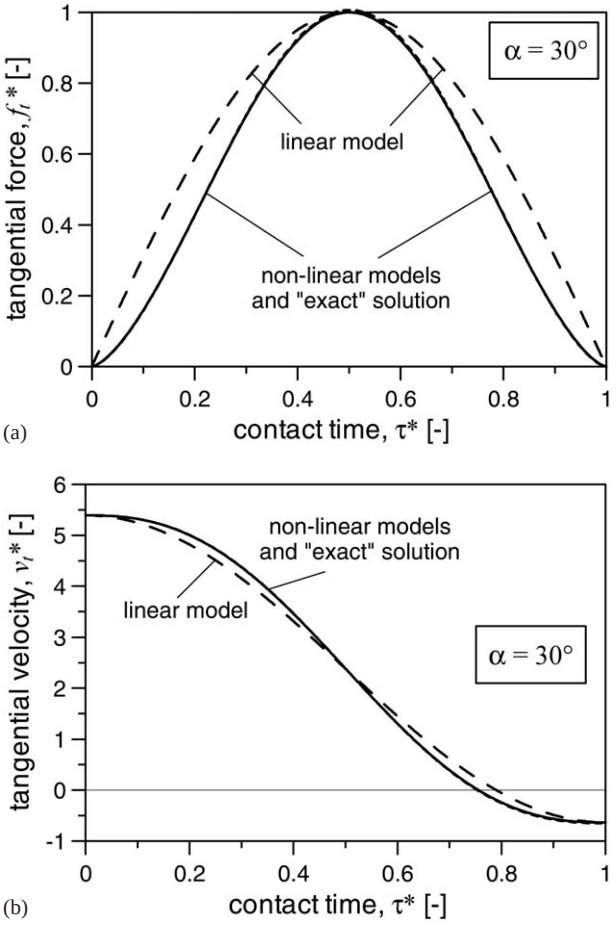

Fig. 15. Evolution of the tangential force (a) and velocity (b) during an impact at 30°.

Fig. 14a shows that during the first half of the collision at $\alpha = 20°$ gross sliding occurs; therefore, all the non-linear models correctly follow the "exact" solution for the tangential force, whereas the linear model shows discrepancies, again mainly due to the effects of a different normal force. It can be demonstrated that the H–MDns model during gross sliding predicts a tangential displacement which is $\frac{2}{3}$ of the actual value. The tangential velocity is well calculated using all the models (Fig. 14b).

At $\alpha = 30°$, as expected, all the impact occurs in gross sliding. At this angle, the non-dimensional tangential force plot is analogous to the corresponding normal force, i.e. all the non-linear models and the exact solution give coincident results and the linear model differs for the functional relation (Fig. 15a). The tangential velocity closely resembles the normal velocity although the values are different (Fig. 15b).

Conclusions very similar to the $\alpha = 30°$ can be drawn for collisions at larger angles, because, as previously mentioned, they lie above the critical angle α_c for this system.

4.4. Choice of the parameter values in the linear model

The method for the evaluation of the parameters in the linear model has not attracted much attention in the literature. It is mentioned that the constants are related to the mechanical properties of the material but none suggests a way to do that. The correct choice of the parameters may be of crucial importance depending on the system to be simulated and it is worth pointing out what are the implications of an improper value for K_n, K_t or μ.

The best criterion for the choice of the parameter values is to calculate them from the actual mechanical properties of the system or to derive them by direct measurements. For example, the friction coefficient μ can be determined by impact experiments similar to those carried out by Kharaz et al. (2001). On the other side, the tangential to normal elastic constant ratio κ can be directly calculated from the Young's modulus and the Poisson ratio of the materials (the appendix). Then, once the normal elastic constant is defined, the tangential elastic constant can be calculated using κ. It must be remarked that the common practice of choosing K_t equal to K_n, i.e. $\kappa = 1$, may influence the simulation performance of the model. Indeed, as an example, the critical angle α_c would result 25° instead of 28°.

A procedure for the determination of the optimal value for the normal constant K_n must be formulated. Materials with

Table 2
Influence of K_n on contact time τ_c and on the maximum absolute value of δ_n, δ_t, f_n and f_t for a collision at $\alpha = 10°$

K_n (N m^{-1})	τ_c (s)	$\delta_n^{(max)}$ (m)	$f_n^{(max)}$ (N)	$\delta_t^{(max)}$ (m)	$f_t^{(max)}$ (N)
1×10^3	1.61×10^{-3}	1.97×10^{-3}	1.97	2.00×10^{-4}	0.13
1×10^4	5.08×10^{-4}	6.21×10^{-4}	6.21	6.32×10^{-5}	0.42
5×10^4	2.27×10^{-4}	2.78×10^{-4}	13.9	2.83×10^{-5}	0.94
1×10^5	1.61×10^{-4}	1.97×10^{-4}	19.7	2.00×10^{-5}	1.32
1×10^6	5.08×10^{-5}	6.21×10^{-5}	62.1	6.32×10^{-6}	4.18
1.72×10^7	1.23×10^{-5}	1.50×10^{-5}	258	1.52×10^{-6}	17.4

smaller elastic constants (softer) were used in many DEM simulations because they allowed larger time step to be used. In fact, by reducing the elastic constant, the contact time ($\tau_c \propto K_n^{-0.5}$) and, consequently, the time step are increased.

Tsuji et al. (1993) reported that numerical experiments proved negligible errors for simulation of fluidized beds when changing the elastic constant of several orders of magnitude. The elastic constant used in their simulation was 800 N m^{-1}. Many authors followed the suggestions of these authors. Xu and Yu (1997) in their work on fluidized-bed DEM simulation claimed to have used a realistic value for the elastic constant ($K_n = 50,000$ N m^{-1}), although this value is orders of magnitude smaller than the value considered in this work. The method proposed in Section 4.1 has an important advantage over other methods: it ensures that the maximum normal force and displacement correspond to the respective values calculated with the non-linear models.

It must be remarked that differences of orders of magnitude are found for all the variables characterizing the collision if a totally unrealistic elastic constant is used. Table 2 reports the contact time τ_c and the maximum absolute value of δ_n, δ_t, f_n and f_t during a collision at $\alpha = 10°$, calculated using the linear model and some values of K_n ranging from 1000 N m^{-1} (close to that used by Tsuji et al., 1993) to the value estimated in Section 4.1. It clearly appears that the variables are proportional to $K_n^{0.5}$ (f_n and f_t) or to $K_n^{-0.5}$ (δ_n and δ_t). Instead, the normal and tangential velocity profiles (and hence, also the velocities at the end of the impact) are independent of K_n. This explains why the simple linear model shows excellent agreement with experimental data, with regard to the final values of the characteristic properties.

The use of a very low K_n can be justified bearing in mind that the main advantage of the linear model is the simplicity and, when the force–displacement interaction is not fundamental, that the larger time step allowed may be very useful for quicker simulations of global granular trajectories. However, care must be taken when assigning arbitrary values, otherwise excessive overlaps are likely to occur. Using 800 N m^{-1} as stiffness constant and the same maximum force calculated in the presented simulations, the resulting normal displacement (overlap) is about 370 mm (74 times the particle diameter!). Moreover, the variation of τ_c implies possible complications if the system to be simulated shows very frequent collisions. In fact, if the granular flow occurs mostly with no collisions, the differences in the contact duration experienced by the particles are hidden by the periods when particles move freely. On the other side, if the stress transmission across multiple contacts is to be studied, i.e. in very contact intensive systems, proper contact duration and force–displacement propagation must be carefully considered. Finally, accurate selection of K_n must be carried out for analyses sensitive to the actual force or displacement. As an example, this is the case of force analyses until particle breakage in comminution or dust formation studies.

5. Conclusions

Three mechanical models for the simulation of elastic frictional collisions were tested for accuracy, comparing the results, microscopically, to nearly exact analytical solutions, and, macroscopically, to experimental results. The analysis could be of interest for people working in the granular motion simulation area, because the models can be used in DEM codes. In order to facilitate the inclusion in this kind of codes, the models were reported in displacement-driven formulation. Particular attention was directed towards the evaluation of the parameters of the linear model.

The macroscopic comparison emphasizes that the agreement of the simple linear model is exceptionally good, indicating that no significant improvements can be attained using the H–MDns and H–MD models. Actually, moving to the H–MDns model is disappointingly worse, especially at low values of the impact angle α. On the microscopic scale, the evolution of the normal and tangential forces, velocities and displacements, predicted by the three models during a collision, were compared with the solution developed by Maw et al. (1976). In these comparisons, the H–MD model provided a better agreement with MBF solution, as expected since all micro-slip effects are correctly accounted for. Instead, the H–MDns model, in principle more detailed than the linear one (and, hence, expected to be better) revealed worse simulation capabilities. However, this happens only if the normal elastic constant K_n, used in the linear model, is carefully evaluated. In fact, using this model, while the velocity profiles are independent of K_n, the contact time and

the actual force and displacement profiles exhibit a dependency from the square root of the normal elastic constant. However, the time scale of the collision process can be of great importance in certain processes, such as multiphase flows, where the response in time of the system is a combination of the characteristic times of the phases involved. Hence, although the discrepancies in the calculated forces and displacements tend to compensate, giving the very good agreement on a macroscopical scale, for analyses sensitive to the actual force or displacement more detailed models such as the H–MD model are necessary. As an example, this is the case of force analyses until particle breakage in dust formation studies.

Notation

a	radius of the contact area, m
C	constant, dimensionless
E	Young's modulus, GPa
f	force, N
G	shear modulus, GPa
I	moment of inertia, kg m^2
K	elastic constant, N m^{-1}
M	mass, kg
n	number of annuli, dimensionless
p	normal stress, Pa
R	radius, m
r	radial coordinate, m
R_g	radius of gyration, dimensionless
t	tangential stress, Pa
v	velocity, m s^{-1}
w_i	coefficients for traction distribution, Pa

Greek letters

α	impact angle, deg
α_c	critical angle, deg
δ	displacement, m
θ	rotation, rad
μ	friction coefficient, dimensionless
ν	Poisson ratio, dimensionless
ρ	density, kg m^{-3}
τ	time, s
τ_c	collision duration, s
χ	geometrical and physical parameter, dimensionless
ψ	non-dimensional tangential velocity of the contact point, dimensionless
ω	rotational velocity, rad s^{-1}

Subscripts

0	initial
eq	equivalent
n	normal
t	tangential

Superscripts

$*$	dimensionless
(SL)	simple loading
(TP)	turning point
(TTP)	second turning point

Appendix

For a collision of two spheres of different materials, the equivalent properties (radius R_{eq}, mass M_{eq}, Young's modulus E_{eq} and shear modulus G_{eq}) in terms of the properties of the single particles i and j are, respectively,

$$R_{eq} = \left(\frac{1}{R_i} + \frac{1}{R_j}\right)^{-1}, \quad M_{eq} = \left(\frac{1}{M_i} + \frac{1}{M_j}\right)^{-1},$$

$$E_{eq} = \left(\frac{1-\nu_i^2}{E_i} + \frac{1-\nu_j^2}{E_j}\right)^{-1},$$

$$G_{eq} = \left(\frac{1-\nu_i}{G_i} + \frac{1-\nu_j}{G_j}\right)^{-1}.$$

For a collision of a sphere i with a wall j, the same relations apply for E_{eq} and G_{eq}, whereas $R_{eq} = R_i$ and $M_{eq} = M_i$. The non-dimensional parameters used in the development of the approximated analytical solution are

$$\psi = \frac{\kappa}{\mu}\frac{v_t}{v_{n_0}}, \quad \chi = \frac{\kappa(1+1/R_g^2)}{2},$$

$$\kappa = \frac{K_{t0}}{K_n} = \frac{(1-\nu_i)/G_i + (1-\nu_j)/G_j}{(1-0.5\nu_i)/G_i + (1-0.5\nu_j)/G_j}.$$

The definition of the non-dimensional variables used in Section 4.3 is

$$\tau^* = \frac{\tau}{\tau_c}, \quad f_n^* = \frac{f_n}{f_n^{(\max)}}, \quad f_t^* = \frac{f_t}{\mu f_n^{(\max)}}, \quad v_n^* = \frac{v_n}{v_{n0}},$$

$$v_t^* = \psi = \frac{\kappa}{\mu}\frac{v_t}{v_{n0}}, \quad \delta_n^* = \frac{\delta_n}{C^2 R_{eq}}, \quad \delta_t^* = \frac{\kappa}{\mu}\frac{\delta_t}{C^2 R_{eq}}.$$

References

Anderson, T.B., Jackson, R., 1967. A fluid mechanical description of fluidized beds. Industrial and Engineering Chemistry Fundamentals 6, 527–539.

Campbell, C.S., Brennen, C.E., 1984. Computer simulation of granular shear flows. Journal of Fluid Mechanics 151, 167–188.

Cleary, P.W., Sawley, M.L., 2002. DEM modelling of industrial granular flows: 3D case studies and the effect of particle shape on hopper discharge. Applied Mathematical Modelling 26, 89–111.

Cundall, P.A., Strack, O.D.L., 1979. A discrete numerical model for granular assemblies. Geotechnique 29, 47–65.

Gera, D., Gautam, M., Tsuji, Y., Kawaguchi, T., Tanaka, T., 1998. Computer simulation of bubbles in large-particle fluidized beds. Powder Technology 98, 38–47.

Hanes, D.M., Walton, O.R., 2000. Simulation and physical measurements of glass spheres flowing down a bumpy incline. Powder Technology 109, 133–144.

Hertz, H., 1882. Über die Berührung fester elastischer Körper (On the contact of elastic solids. Journal fur die Reine und Angewandte Mathematik 92, 156–171.

Hoomans, B.P.B., Kuipers, J.A.M., Briels, W.J., Van Swaaij, P.M., 1996. Discrete particle simulation of bubble and slug formation in a two-dimensional gas-fluidised bed: a hard-sphere approach. Chemical Engineering Science 51 (1), 99–118.

Huilin, L., Yurong, H., Gidaspow, D., 2003. Hydrodynamic modelling of binary mixture in a gas bubbling fluidized bed using the kinetic theory of granular flow. Chemical Engineering Science 58, 1197–1205.

Johnson, K.L., 1985. Contact Mechanics. Cambridge University Press, Cambridge.

Kafui, K.D., Thornton, C., Adams, M.J., 2002. Discrete particle-continuum fluid modelling of gas–solid fluidised beds. Chemical Engineering Science 57, 2395–2410.

Kawaguchi, T., Tanaka, T., Tsuji, Y., 1998. Numerical simulation of two-dimensional fluidized beds using the discrete element method (comparison between the two- and the three-dimensional models). Powder Technology 96, 129–138.

Kawaguchi, T., Sakamoto, M., Tanaka, T., Tsuji, Y., 2000. Quasi-three-dimensional numerical simulation of spouted beds in cylinder. Powder Technology 109, 3–12.

Kharaz, A.H., Gorham, D.A., Salman, A.D., 2001. An experimental study of the elastic rebound of spheres. Powder Technology 120, 281–291.

Langston, P.A., Tüzün, U., Heyes, D.M., 1995. Discrete element simulation of granular flow in 2D and 3D hoppers: dependence of discharge rate and wall stress on particle interactions. Chemical Engineering Science 50, 967–987.

Li, J., Kuipers, J.A.M., 2003. Gas–particle interactions in dense gas-fluidized beds. Chemical Engineering Science 58, 711–718.

Maw, N., Barber, J.R., Fawcett, J.N., 1976. The oblique impact of elastic spheres. Wear 38, 101–114.

McKeen, T., Pugsley, T., 2003. Simulation and experimental validation of a freely bubbling bed of FCC catalyst. Powder Technology 129, 139–152.

Mikami, T., Kamiya, H., Horio, M., 1998. Numerical simulation of cohesive powder behavior in a fluidized bed. Chemical Engineering Science 53 (10), 1927–1940.

Mindlin, R.D., Deresiewicz, H., 1953. Elastic spheres in contact under varying oblique forces. Transactions of ASME, Series E. Journal of Applied Mechanics 20, 327–344.

Mishra, B.K., Murty, C.V.R., 2001. On the determination of contact parameters for realistic DEM simulations of ball mills. Powder Technology 115, 290–297.

Moreno, R., Ghadiri, M., Antony, S.J., 2003. Effect of the impact angle on the breakage of agglomerates: a numerical study using DEM. Powder Technology 130, 132–137.

Nase, S.T., Watson, L.V., Adetola, A.A., McCarthy, J.J., 2001. Discrete characterization tools for cohesive granular material. Powder Technology 116, 214–223.

Pain, C.C., Mansoorzadeh, S., Gomes, J.L.M., de Oliveira, C.R.E., 2002. A numerical investigation of bubbling gas–solid fluidized bed dynamics in 2-D geometries. Powder Technology 128, 56–77.

Peirano, E., Delloume, V., Johnsson, F., Leckner, B., Simonin, O., 2002. Numerical Simulation of the fluid dynamics of a freely bubbling fluidized bed: influence of the air supply system. Powder Technology 122, 69–82.

Rhodes, M.J., Wang, X.S., Nguyen, M., Stewart, P., Liffman, K., 2001. Onset of cohesive behaviour in gas fluidized beds: a numerical study using DEM simulation. Chemical Engineering Science 56, 4433–4438.

Rong, D.G., Mikami, T., Horio, M., 1999. Particle and bubble movements around tubes immersed in fluidized beds—a numerical study. Chemical Engineering Science 54, 5737–5754.

Sadd, M.H., Tai, Q., Shukla, A., 1993. Contact law effects on wave propagation in particulate materials using distinct element modeling. International Journal of Non-Linear Mechanics 28, 251–265.

Syamlal, M., Rodgers, W., O'Brien, T.J., 1993. MFIX Documentation: Theory Guide. Technical Note, DOE/METC-94/1004.

Tanaka, K., Nishida, M., Kunimochi, T., Takagi, T., 2002. Discrete element simulation and experiment for dynamic response of two-dimensional granular matter to the impact of a spherical projectile. Powder Technology 124, 160–173.

Thornton, C., 1997. Coefficient of restitution for collinear collisions of elastic-perfectly plastic spheres. Journal of Applied Mechanics 64, 383–386.

Thornton, C., Yin, K.K., 1991. Impact of elastic spheres with and without adhesion. Powder Technology 65, 153–166.

Tsuji, Y., Tanaka, T., Ishida, T., 1992. Lagrangian numerical simulation of plug flow of cohesionless particles in a horizontal pipe. Powder Technology 71, 239–250.

Tsuji, Y., Kawaguchi, T., Tanaka, T., 1993. Discrete particle simulation of two-dimensional fluidized bed. Powder Technology 77, 79–87.

Tsuji, Y., Tanaka, T., Yonemura, S., 1998. Cluster patterns in circulating fluidized beds predicted by numerical simulation (discrete particle model versus two-fluid model). Powder Technology 95, 254–264.

Venugopal, R., Rajamani, R.K., 2001. 3D simulation of charge motion in tumbling mills by the discrete element method. Powder Technology 115, 157–166.

Vu-Quoc, L., Zhang, X., 1999. An accurate and efficient tangential force–displacement model for elastic frictional contact in particle-flow simulations. Mechanics of Materials 31, 235–269.

Vu-Quoc, L., Zhang, X., Walton, O.R., 2000. A 3-D discrete-element method for dry granular flows of ellipsoidal particles. Computer Methods in Applied Mechanics and Engineering 187, 483–528.

Vu-Quoc, L., Zhang, X., Lesburg, L., 2001. Normal and tangential force–displacement relations for frictional elasto-plastic contact of spheres. International Journal of Solids and Structures 38, 6455–6489.

Walton, O.R., Braun, R.L., 1986. Viscosity, granular-temperature, and stress calculations for shearing assemblies of inelastic, frictional disks. Journal of Rheology 30, 949–980.

Xu, B.H., Yu, A.B., 1997. Numerical simulation of the gas-solid flow in a fluidized bed by combining discrete particle method with computational fluid dynamics. Chemical Engineering Science 52, 2785–2809.

Xu, B.H., Yu, A.B., Chew, S.J., Zulli, P., 2000. Numerical simulation of the gas–solid flow in a bed with lateral gas blasting. Powder Technology 109, 13–26.